Journal of Computational Physics 509 (2024) 113028

Contents lists available at ScienceDirect

Journal of Computational Physics

journal homepage: www.elsevier.com/locate/jcp

A boundary condition-enhanced direct-forcing immersed boundary method for simulations of three-dimensional phoretic particles in incompressible flows

Xiaojue Zhu [a,*,1], Yibo Chen [b,1], Kai Leong Chong [c], Detlef Lohse [b,d], Roberto Verzicco [e,b,f]

[a] Max Planck Institute for Solar System Research, 37077 Göttingen, Germany
[b] Physics of Fluids Group, Max Planck Center Twente for Complex Fluid Dynamics, and J. M. Burgers Centre for Fluid Dynamics, University of Twente, P.O. Box 217, 7500AE Enschede, Netherlands
[c] Shanghai Institute of Applied Mathematics and Mechanics, School of Mechanics and Engineering Science, Shanghai University, Shanghai, 200072, China
[d] Max Planck Institute for Dynamics and Self-Organization, 37077 Göttingen, Germany
[e] Department of Industrial Engineering, University of Rome 'Tor Vergata', Via del Politecnico 1, Roma 00133, Italy
[f] Gran Sasso Science Institute–Viale F. Crispi, 7 67100 L'Aquila, Italy

ARTICLE INFO

Keywords:
Immersed boundary method
Phoretic particles
Janus particles
Neumann boundary condition

ABSTRACT

In this paper we propose an improved three-dimensional immersed boundary method coupled with a finite-difference code to simulate self-propelled phoretic particles in viscous incompressible flows. We focus on the phenomenon of diffusiophoresis which, using the driving of a concentration gradient, can generate a slip velocity on a surface. In such a system, both the Dirichlet and Neumann boundary conditions are involved. In order to enforce the boundary conditions, we propose two improvements to the basic direct-forcing immersed boundary method. The main idea is that the immersed boundary terms are corrected by adding the force of the previous time step, in contrast to the traditional method which relies only on the instantaneous forces in each time step. For the Neumann boundary condition, we add two auxiliary layers inside the body to precisely implement the desired concentration gradient. To verify the accuracy of the improved method, we present problems of different complexity: The first is the pure diffusion around a sphere with Dirichlet and Neumann boundary conditions. Then we show the flow past a fixed sphere. In addition, the motion of a self-propelled Janus particle in the bulk and the spontaneously symmetry breaking of an isotropic phoretic particle are reported. The results are in very good agreements with the data that are reported in previously published literature.

1. Introduction

Active matter has attracted a great attention in recent years from experimental and theoretical perspectives [1–5], owing to its potential vast applications in drug delivery, medical treatment and other lab-on-a-chip devices. Interfacial phoretic effects have

* Corresponding author.
E-mail address: zhux@mps.mpg.de (X. Zhu).
[1] These authors have made an equal contribution to the manuscript.

https://doi.org/10.1016/j.jcp.2024.113028
Received 26 October 2023; Received in revised form 11 April 2024; Accepted 15 April 2024

Available online 19 April 2024

shown an effective and promising strategy in designing such artificial micro-scale active swimmers, by which the locally generated concentration gradient drives the motion of the objects in fluids [6–9]. Self-phoretic swimmers are typically composed of two parts: a functional part which modifies the surrounding solvent properties and creates a local gradient field, and a non-functional part which is exposed then to the local gradient field. Most existing investigations on the self-phoretic microswimmers consider Janus particles, which can be easily synthesized using partial metal coating on colloidal spheres [10] (see the sketch of a Janus particle in Fig. 1). In diffusiophoretic microswimmers, the metal coated part catalyzes a chemical reaction, inducing a local concentration gradient, which then drives self-propulsion.

The extensive experimental and theoretical studies on phoretic particles have greatly improved our understandings towards the dynamics of single and collective behavior of phoretic particles. For more details on the recent development of phoretic self-propulsion, we refer the readers to the reviews by Maass et al. [11], Moran and Posner [7], Illien et al. [8], and Michelin [9]. From the numerical side, the studies are more scarce and two alternative approaches are possible: microscopic (discrete) methods allow to describe the behavior of individual particles for a very short time evolution starting from the specific molecular mechanisms. In contrast, macroscopic (continuum) descriptions permit the simulation of systems of many particles in complex environments for longer evolution times. The price to pay in this second case is that all the microscopic mechanisms are lumped in an effective boundary condition. So far, most of the simulations have adopted particle based microscopic discrete models in two dimensions. For example, one of the popular methods is the Brownian dynamics method which has been used to simulate the Brownian motion of Janus particles by integrating the Langevin equations [12–16]; other methods that are widely used are molecular dynamics simulations [17–19], which can become computationally very expensive when considering many molecules; and the direct simulation Monte Carlo method [20,21], for which the convergence can be slow and statistical noise large. Recently, a hybrid method has been proposed that describes the solvent by a coarse-grained particle-based method, while the interactions of the Janus particle with the solvent are simulated by standard molecular dynamics [22,23]. The advantage of the method is that it captures the combined effects of Brownian and hydrodynamic forces. However, we note that most physical models of self-diffusiophoresis consider the particle and surrounding solution at the macroscopic level, with a constitutive model for the reactions at the surface that generates the concentration gradient [6,7,9]. The molecular interaction at the interface is simplified by a slip velocity.

In this manuscript we adopt direct numerical simulations (DNS), with the strict accordance to these continuum models, to simulate the motions of phoretic particles. Compared with the microscopic methods mentioned above, DNS is an effective model [24–26] that offers a chance to efficiently deal with larger scale problems and more complicated configurations. The difficulties of DNS for phoretic particles lie in how to treat the moving boundaries and the complex boundary conditions (Neumann boundary conditions). In Stokes flow, spherical harmonic expansion and boundary integral method have been used to discretize the Stokes equations [27,28]. Here we choose the immersed boundary method (IBM), which has been widely used in the literature to deal with fluid structure interactions, mainly due to its capability of solving flows with complex and moving boundaries on simple Cartesian meshes at arbitrary Reynolds numbers. In this work, IBM has been adopted to simulate flows with phoretic particles [29,30]. IBM was first introduced by Peskin [31] in 1972 to simulate heart flow. Since then, many variants have been developed [32–35]. Still, the basic ideas are the same: a body force is added to the momentum equation to enforce the desired boundary conditions using a non body-fitted mesh. Nowadays, IBM is applied not only to biological flows [36–39], but also to particulate flows [40–44], flows with surface roughness [32,45–48], and heat transfer problems [49–54].

IBM can be classified into two types: continuous-forcing and direct-forcing [33]. In the continuous-forcing approach, the forcing is incorporated into the continuous equations before discretization whereas in the direct-forcing approach, the forcing is introduced after the equations are discretized. Alternatively, IBM can also be classified depending on the boundary conditions: those for Dirichlet boundary conditions and those for Neumann boundary conditions. For more details on the continuous-forcing and direct-forcing IBM for Dirichlet boundary conditions, we refer the readers to the reviews [32–34]. As compared to Dirichlet boundary condition, Neumann boundary condition presents a harder challenge and so far only a few studies have been undertaken. Zhang et al. [50] proposed an auxiliary layer of Lagrangian points outside the boundary to calculate the surface temperature from the gradient. Toja-Silva et al. [55] proposed a radial basis function to deal with interpolation and spreading for both Dirichlet and Neumann type conditions. Luo et al. [52] introduced two points outside the boundary to calculate the temperature inside the boundary. Wang et al. [53] utilized two layers of discrete Lagrangian points that respectively placed inside and outside of the solid body with a distance of two grid spacings, to calculate temperature corrections implicitly on the boundary. Wu et al. [56] also put two auxiliary layers (one inside and one outside the solid boundary) to enhance the Neumann boundary condition with explicit method.

In this manuscript, we introduce an improved direct-forcing immersed boundary method for simulations of three-dimensional phoretic particles in incompressible viscous flows. Unlike the existing direct-forcing method [57,40] that calculates the full Lagrangian forces in each time step, we compute the actual Lagrangian forces by adding a correction to the force of the previous time step. By doing so, the boundary condition can be satisfied with a greater precision. This method can be thought of as the analogue of the pressure correction in fractional step method that has been widely used in last three decades in comparison to the total pressure calculation from the original projection method [58]. We note that there are other works in literature that improves the precision by adding corrections to forcing, e.g. [59,60] The other improvement is that we add two more auxiliary layers of Lagrangian points inside the sphere to precisely implement the desired Neumann boundary condition. The performance of the proposed IBM are tested and validated by several benchmarks, ranging from phoretic particle to flow past spheres and spontaneously symmetry breaking phoretic particles.

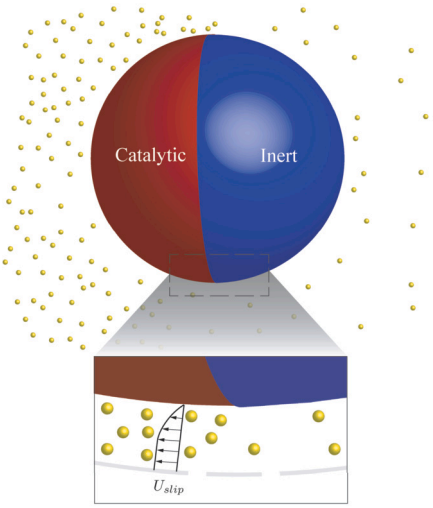

Fig. 1. Schematic description of a Janus particle, which is typically composed of two parts: a functional (catalytic) part which modifies the surrounding solvent properties and creates a local gradient field, and a non-functional (inert) part which is exposed then to the local gradient field. The concentration gradient drives the slip velocity of the particle.

2. Governing equations and numerical schemes

2.1. Governing equations

The self-propulsion of phoretic particles is driven by diffusiophoresis. This can be achieved by a particle whose surface is divided into two parts, one coated by catalyst, and the other by inert material. Owing to chemical reactions, molecules or ions are released at the catalytic side, producing a concentration gradient along the surface and driving the motion of the particle, as shown in Fig. 1.

Note that all dimensional physical variables are marked with tildes (e.g. $\tilde{c}$, $\tilde{\boldsymbol{u}}$), while the dimensionless ones without (e.g. c, $\boldsymbol{u}$). The control parameter is the strength α of the reaction activity at the catalytic surface, i.e. the generation or consumption of solute by the reaction. With the diffusion coefficient D, the concentration boundary condition is then:

$$D\frac{\partial \tilde{c}}{\partial \tilde{n}} = \alpha, \tag{1}$$

where $\frac{\partial \tilde{c}}{\partial \tilde{n}}$ is the gradient at the boundary in the wall-normal direction.

Due to the diffusiophoretic effect, the slip velocity is proportional to the tangential concentration gradient:

$$\tilde{\mathbf{u}}_s = M(\mathbf{I} - \mathbf{nn}) \cdot \nabla \tilde{c}, \tag{2}$$

where M is the diffusiophoretic mobility, which is a constant in our case [25], $\tilde{\mathbf{u}}_s$ the slip velocity, $\mathbf{I}$ the identity tensor, and $(\mathbf{I} - \mathbf{nn})$ scalarly multiplied by $\nabla \tilde{c}$ yields the tangential component of the concentration gradient.

With the parameters mentioned above and the diameter of the particle L, we can define the characteristic length, velocity, concentration as L, $\alpha M/D$, $\alpha L/D$, respectively.

The concentration field is governed by the diffusion-convection equation and the flow dynamics are described by the Navier-Stokes equations. The dimensionless form of the governing equations becomes:

$$\frac{\partial c}{\partial t} + \mathbf{u} \cdot \nabla c = \frac{1}{Pe}\nabla^2 c, \tag{3}$$

$$\frac{\partial \boldsymbol{u}}{\partial t} + (\boldsymbol{u} \cdot \nabla)\boldsymbol{u} = -\nabla p + \frac{Sc}{Pe}\nabla^2 \boldsymbol{u}, \quad \boldsymbol{\nabla} \cdot \boldsymbol{u} = 0, \tag{4a,b}$$

where the Schmidt Sc and the Péclet Pe numbers are defined as [24]:

$$Pe = \frac{M\alpha L}{D^2}, \quad Sc = \frac{\nu}{D}. \tag{5a,b}$$

The inert part of the surface, being a simple impermeable wall, is modeled by a Neumann boundary condition with zero chemical reaction, while in contrast, reaction product emits from the catalytic surface:

$$\frac{\partial c}{\partial n} = 0, \text{ at the inert surface;} \quad \frac{\partial c}{\partial n} = 1, \text{ at the catalytic surface.} \tag{6a,b}$$

The concentration gradient drives a slip motion at the surface [24,25],

$$\mathbf{u}_s = (\mathbf{I} - \mathbf{nn}) \cdot \nabla c, \tag{7}$$

which is the dimensionless form of Equation (2).

The flow velocity on the boundaries is the summation between the particle and slip velocities [25]

$$\mathbf{U}^b(\mathbf{x},t) = \mathbf{U} + \boldsymbol{\omega} \times (\mathbf{x}_s - \mathbf{x}_0) + \mathbf{u}_s. \tag{8}$$

Here $\mathbf{U}$ is the particle translation velocity, $\boldsymbol{\omega}$ its angular velocity, $\mathbf{x}_s$ and $\mathbf{x}_0$ the spatial positions of the particle surface and center of rotation, respectively.

The translational and angular velocities are determined by the following relations:

$$m_p \frac{d\mathbf{U}}{dt} = \mathbf{F}_p, \quad I_p \frac{d\boldsymbol{\omega}}{dt} = \mathbf{T}_p, \tag{9a,b}$$

where m_p and I_p are the mass and moment of inertia of the particle, respectively. $\mathbf{F}_p$ and $\mathbf{T}_p$ are the force and torque exerted on the particle by the fluids:

$$\mathbf{F}_p = \int \boldsymbol{\sigma} \cdot \mathbf{n} dS = \int (p\mathbf{I} + \frac{Sc}{Pe}(\nabla \mathbf{u} + (\nabla \mathbf{u})^T)) \cdot \mathbf{n} dS, \tag{10}$$

$$\mathbf{T}_p = \int (\mathbf{x}_s - \mathbf{x}_0) \times (\boldsymbol{\sigma} \cdot \mathbf{n}) dS, \tag{11}$$

where $\boldsymbol{\sigma}$ is the hydrodynamic stress tensor. Equations (3)-(11) all together govern the dynamics of fluid, phoretic particles and their interactions.

2.2. Fundamentals of immersed boundary method

In this section, we will shortly summarize the immersed boundary method in [39,61] in order to make the manuscript self-consistent. To deal with the moving boundary, a moving Lagrangian grid, attached to the surface of the solid particle is applied while the fluid phase is solved on a fixed and staggered Cartesian grid. Note that from now on, we will use capital letters to represent the quantities on the Lagrangian markers (solid body), whereas lower cases to represent the quantities on the Eulerian meshes (fluid domain).

In the IBM by Tullio and Pascazio [39] and Spandan et al. [61], the viscous term is discretized based on the Crank-Nicolson scheme. With the explicit three-step Runge-Kutta time advancement scheme, the detailed discrete equations can be written as:
do $i = 1, 3$

$$\frac{\hat{\mathbf{u}} - \mathbf{u}^i}{\Delta t} = \alpha_i \nabla p^i + \gamma_i \mathbf{H}_u^i + \rho_i \mathbf{H}_u^{i-1} + \frac{\alpha_i}{2} \frac{Sc}{Pe} \nabla^2 (\hat{\mathbf{u}} + \mathbf{u}^i), \tag{12}$$

$$\mathbf{u}^* = \hat{\mathbf{u}} + \mathbf{f}^i \Delta t, \tag{13}$$

$$\nabla^2 \hat{p} = \frac{\nabla \cdot \mathbf{u}^*}{\alpha_i \Delta t}, \tag{14}$$

$$\mathbf{u}^{i+1} = \mathbf{u}^* - \alpha_i \Delta t \nabla \hat{p}, \tag{15}$$

$$p^{i+1} = p^i + \hat{p} - \frac{\alpha_i \Delta t}{2} \frac{Sc}{Pe} \nabla^2 \hat{p}. \tag{16}$$

enddo

$\mathbf{H}_u$ denotes the nonlinear explicit (advection) terms, discretized with the Adams-Bashforth scheme. α_i, γ_i and ρ_i are the coefficients of the three steps Runge-Kutta time advancement scheme, which we apply the same values as [62]. $\mathbf{f}$ is the forcing term for the velocity field.

We have implemented the concentration field in a similar way:
do $i = 1, 3$

$$\frac{\hat{c} - c^i}{\Delta t} = \gamma_i H_c^i + \rho_i H_c^{i-1} + \frac{\alpha_i}{2Pe} \nabla^2 (\hat{c} + c^i), \tag{17}$$

$$c^{i+1} = \hat{c} + s^i \Delta t, \tag{18}$$

enddo

where H_c is the advection term and s is the forcing term for concentration.

The forcing term for velocity is calculated as follows:

$$\text{Interpolation: } \hat{\mathbf{U}}(\mathbf{X}) = \sum_{k=1}^{N_e} \phi_k^l(\mathbf{X}) \hat{\mathbf{u}}^i, \tag{19}$$

$$\text{Forcing: } \mathbf{F} = \frac{\mathbf{U}^b - \hat{\mathbf{U}}}{\Delta t}, \tag{20}$$

$$\text{Spreading: } \mathbf{f}^i = \sum_{l=1}^{N_l} r_l \phi_k^l(\mathbf{X}) \mathbf{F}_l, \tag{21}$$

r_l is the ratio between the Lagrangian and Eulerian grid volume. The coefficient ϕ_k is calculated based on the Moving Least Square (MLS) method, which is explained in detail in [39,61]. k is the index for the Eulerian points and l is the index for the Lagrangian points.

Concentration and velocity forcing can be calculated using exactly the same method. For concentration field, Neumann boundary condition has to be considered and a single outer probe at distance of grid size from surface is applied (Fig. 2(a)). Note that in this manuscript, the Cartesian grid around the particle is always uniform in all three directions. The forcing term is added on the Lagrangian grids at the surface. For unit concentration gradient ($\frac{\partial c}{\partial n} = 1$, catalytic surface), the intended concentration C_I at the surface is:

$$C_I = C_p + h, \tag{22}$$

where C_p is the concentration at the outer probe. h is the width of the Eulerian mesh. For zero concentration gradient ($\frac{\partial c}{\partial n} = 0$, inert surface), $C_I = C_p$. As a consequence, the forcing term for concentration is calculated as:

$$\text{Interpolation: } \hat{C}(\mathbf{X}) = \sum_{k=1}^{N_e} \phi_k^l(\mathbf{X})\hat{c}^i, \tag{23}$$

$$\text{Forcing: } S = \frac{C_I - \hat{C}}{\Delta t}, \tag{24}$$

$$\text{Spreading: } s^i = \sum_{l=1}^{N_l} r_l \phi_k^l(\mathbf{X}) S_l. \tag{25}$$

The force and torque acting on the particle can be expressed as in [40]:

$$\rho_p V_p \frac{d\mathbf{U}}{dt} = -\rho_f \sum_{l=1}^{N_l} \mathbf{F}^l \Delta V^l + \rho_f \frac{d}{dt}\left(\int_{V_p} \mathbf{u} dV\right), \tag{26}$$

$$I_p \frac{d\boldsymbol{\omega}}{dt} = -\rho_f \sum_{l=1}^{N_l} \mathbf{r}^l \times \mathbf{F}^l \Delta V^l + \rho_f \frac{d}{dt}\left(\int_{V_p} \mathbf{r} \times \mathbf{u} dV\right), \tag{27}$$

where the subscript f represents the parameter for fluids and p for particle. ρ is density. ΔV^l is the volume of lth Lagrangian grid cell.

2.3. Improvements to the original immersed boundary method

2.3.1. Forcing error

The original method [39,61] does not exactly impose the desired boundary condition, rather, velocity and concentration errors remain (see an example in Fig. 4). Following a similar analysis as in [42,63] (based on the IBM by Uhlmann [40]), here we show why the error exists. The exact implicit forcing $\mathbf{f}^{(i)}$ required to yield a desired velocity $\mathbf{u}^d$ reads

$$\mathbf{f}^{(i)} = \frac{\mathbf{u}^d - \mathbf{u}^i}{\Delta t} - \frac{\alpha_i Sc}{Pe}\nabla^2(\mathbf{u}^d + \mathbf{u}^i) - \mathbf{C}^i, \tag{28}$$

where the pressure and the explicit terms are lumped into $\mathbf{C}^i$ for simplicity. However, the explicit forcing in [39,61] is in fact calculated using

$$\mathbf{f}^{(e)} = \frac{\mathbf{u}^d - \mathbf{u}^i}{\Delta t} - \frac{\alpha_i Sc}{Pe}\nabla^2(\hat{\mathbf{u}} + \mathbf{u}^i) - \mathbf{C}^i. \tag{29}$$

Therefore, the forcing error $\Delta\mathbf{f} = \mathbf{f}^{(i)} - \mathbf{f}^{(e)}$ is given by

$$\Delta\mathbf{f} = \frac{\alpha_i Sc}{Pe}\nabla^2(\hat{\mathbf{u}} - \mathbf{u}^d), \tag{30}$$

or

$$(1 - \frac{\Delta t \alpha_i Sc}{2Pe})\Delta\mathbf{f} = -\frac{\alpha_i Sc}{Pe}\nabla^2(\Delta t\mathbf{C}^i + \frac{\Delta t \alpha_i Sc}{Pe}\nabla^2\mathbf{u}^i + \Delta t\mathbf{f}^{(e)}). \tag{31}$$

It can be easily seen that the forcing error is dependent on the Reynolds number ($Re = Pe/Sc$), and time step, as shown in [42]. The other interesting fact to note is that if the intermediate velocity is closer to the desired velocity, then the forcing error will be smaller.

2.3.2. New forcing scheme

We now show how we can improve the forcing through a simple and efficient way. To deal with the forcing error, multidirect forcing scheme was applied as a remedy in [42], which calculate the force in multiple substeps inside an additional forcing loop.

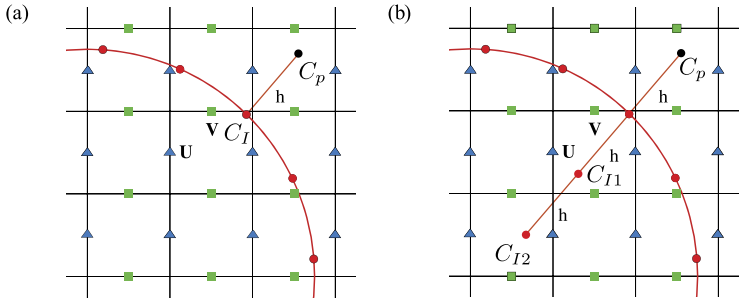

Fig. 2. For the Neumann boundary condition, (a) the original way of obtaining the surface concentration, using only one layer of Lagrangian points, with the help of the probe from outside the boundary. (b) an improved way, using two inner layers of Lagrangian points inside the sphere, with the same normal concentration gradients among these layers. The probe length is the same as the grid size h.

The precision and efficiency are dependent on the number of the substeps. In comparison, here we present a new forcing scheme, in which the intermediate velocity $\hat{\mathbf{u}}$ is calculated by adding the body force from the last time step into Equation (12) and the IBM forces are now given by:

$$\text{Interpolation: } \hat{\mathbf{U}}(\mathbf{X}) = \sum_{k=1}^{N_e} \phi_k^l(\mathbf{X})\hat{\mathbf{u}}^i, \tag{32}$$

$$\text{Forcing: } \mathbf{F}^i = \frac{\mathbf{U}^b - \hat{\mathbf{U}}}{\Delta t} + \mathbf{F}^{i-1}, \tag{33}$$

$$\text{Spreading: } \mathbf{f}^i = \sum_{l=1}^{N_l} r_l \phi_k^l(\mathbf{X})\mathbf{F}_l^i. \tag{34}$$

The concentration forcing term is calculated in the same way in the improved method. The method does not need extra steps to calculate the force and can achieve much better precision, which will be shown in section 3. The underlying principle behind the effectiveness of this straightforward approach lies in the fact that, during the computation of the intermediate velocity $\hat{\mathbf{u}}$, the inclusion of the body force term on the right-hand side significantly aligns it with the desired velocity $\mathbf{u}^d$, as opposed to when the body force term is omitted. With this method, the forcing error becomes

$$(1 - \frac{\Delta t \alpha_i Sc}{2Pe})\Delta\mathbf{f} = -\frac{\alpha_i Sc}{Pe}\nabla^2(\Delta t\mathbf{C}^i + \frac{\Delta t \alpha_i Sc}{Pe}\nabla^2\mathbf{u}^i + \Delta t\mathbf{f}_{i+1}^{(e)} - \Delta t\mathbf{f}_i^{(e)}). \tag{35}$$

Hence, the discrepancy introduced by explicit forcing will be notably diminished when the force undergoes minimal variations between consecutive time steps.

Another implication of the discussion here is that employing a full explicit discretization of the diffusion term leads to a reduction in boundary error, albeit not its complete elimination. This persistence of error is attributable not only to the inherent forcing error but also to the interpolation of velocity and concentration fields, along with the spreading of forcing in discrete form, inevitably introducing additional errors. To elucidate this matter, consider the process where the Lagrangian force $\mathbf{F}$ is dispersed onto Eulerian points and subsequently interpolated back to the Lagrangian points. Spreading

$$\mathbf{f} = \sum_{l=1}^{N_l} r_l \phi_k^l(\mathbf{X})\mathbf{F}_l. \tag{36}$$

Interpolation produces the values $\mathbf{F}^*$ at the Lagrangian points, where

$$\mathbf{F}^*(\mathbf{X}) = \sum_{k=1}^{N_e} \phi_k^l(\mathbf{X})\mathbf{f}. \tag{37}$$

Inserting equation (36) into (37), we get,

$$\mathbf{F}^*(\mathbf{X}) = \sum_{k=1}^{N_e}\sum_{l=1}^{N_l} r_l \phi_k^l(\mathbf{X})\phi_k^l(\mathbf{X})\mathbf{F}_l. \tag{38}$$

It's worth noting that since the function ϕ_k^l is regularized, akin to a smoothed delta function, it's evident that $\phi_k^l \cdot \phi_k^l \neq \phi_k^l$, hence $\mathbf{F}^* \neq \mathbf{F}$. A portion of the forcing error also stems from this phenomenon. A test case of explicit diffusion term is given in subsection 3.1.1, which reduces the boundary error even further, however, it was not entirely eliminated. Note that we will not use it in the other parts of the manuscript because explicit diffusion term requires very small time step.

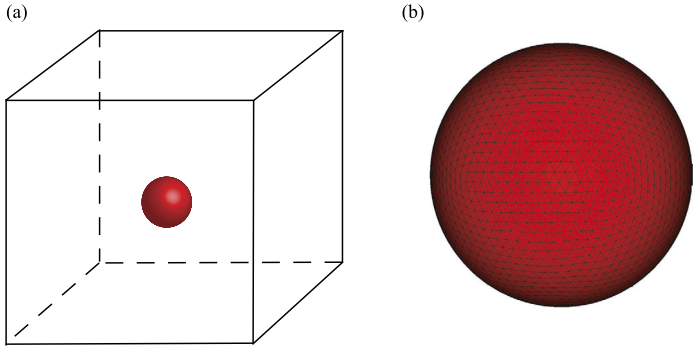

Fig. 3. (a) Setup for the tests performed in section 3.1.1 and section 3.1.3. The size of the domain is $10 \times 10 \times 10$ of the sphere diameter and the grid resolution is $192 \times 192 \times 192$. The sphere locates at the center of the domain. (b) The sphere is discretized into 5120 triangles and the Lagrangian grid size is around 0.7 times of the Eulerian one.

2.3.3. Two-inner-probe method

For the concentration field, the simple one probe method in the previous section cannot guarantee the precision near the interface (which are thoroughly discussed in section 3.1) in the cases with the Neumann boundary condition. In this section, we present a two-inner-probe method, which is shown in Fig. 2(b). The overall arrangement is such to have one layer of probes (P) outside and two layers ($I1$, $I2$) inside the body. The concentration forcing terms, which are calculated based on the interpolated concentration at the outer probe, are added at two inner probes. For unit concentration gradient, the prescribed concentration at the two inner probes are calculated by:

$$C_{I1} = C_p + 2h, \quad C_{I2} = C_p + 3h, \tag{39a,b}$$

where C_p is the concentration at outer probe and C_{I1}, C_{I2} are two inner probes. C_{I1} and C_{I2} are the prescribed concentration boundary conditions. By adding forcing on C_{I1} and C_{I2}, we ensure adherence to the Neumann boundary condition on C_I.This way the concentration gradient at the normal direction of the surface is continuous, making an improvement to the satisfaction of the boundary condition.

2.4. Numerical method

Throughout the manuscript, the fluid solver is based on our recently developed massively parallelized code AFiD [64–66]. The code has been used extensively recently to study rotating turbulence and thermal convection [46–48,54,67–69]. In the code, the Navier–Stokes equations are discretized by central second-order finite-difference schemes on a staggered mesh and the resulting system is solved by a fractional-step method [58,62,64]. The governing equations are discretized by Crank-Nicolson scheme for the viscous terms and an explicit three-step Runge-Kutta scheme for the remaining ones. The time advancement of the solution is:
do $i = 1, 3$

$$\frac{\hat{c} - c^i}{\Delta t} = \gamma_i H_c^i + \rho_i H_c^{i-1} + \frac{\alpha_1}{2Pe}\nabla^2(\hat{c} + c^i) + s^{i-1}, \tag{40}$$

$$\frac{\hat{\mathbf{u}} - \mathbf{u}^i}{\Delta t} = \alpha_i \nabla p^i + \gamma_i \mathbf{H}_u^i + \rho_i \mathbf{H}_u^{i-1} + \frac{\alpha_i}{2}\frac{Sc}{Pe}\nabla^2(\hat{\mathbf{u}} + \mathbf{u}^i) + \mathbf{f}^{i-1}, \tag{41}$$

$$\hat{C} = \sum_{k=1}^{N_e} \phi_k^l(\mathbf{X})\hat{c}, \tag{42}$$

$$\hat{\mathbf{U}} = \sum_{k=1}^{N_e} \phi_k^l(\mathbf{X})\hat{\mathbf{u}}, \tag{43}$$

$$S^i = \frac{C_I - \hat{C}}{\Delta t} + S^{i-1}, \tag{44}$$

$$\mathbf{F}^i = \frac{\mathbf{U}^b - \hat{\mathbf{U}}}{\Delta t} + \mathbf{F}^{i-1}, \tag{45}$$

$$s^i = \sum_{l=1}^{N_l} r_l \phi_k^l(\mathbf{X}) S_l^i, \tag{46}$$

$$\mathbf{f}^i = \sum_{l=1}^{N_l} r_l \phi_k^l(\mathbf{X}) \mathbf{F}_l^i, \tag{47}$$

$$c^{i+1} = \hat{c} + s^i \Delta t, \tag{48}$$

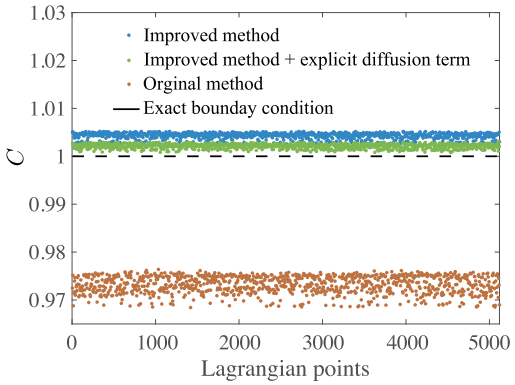

Fig. 4. Concentration on the surface points of a stationary particle with Dirichlet boundary condition $C = 1$ for original (red), improved (blue), and improved method with explicit diffusion term (green). It can be seen that the results of improved forcing method satisfies the boundary condition much better than that of the original method. With explicit diffusion term, the error can be reduced even further. The parameters are $Sc = 510$ and $Pe = 8.45 \times 10^{-3}$. (For interpretation of the colors in the figure(s), the reader is referred to the web version of this article.)

$$\mathbf{u}^* = \hat{\mathbf{u}} + \mathbf{f}^i \Delta t, \tag{49}$$

$$\nabla^2 \hat{p} = \frac{\nabla \cdot \mathbf{u}^*}{\alpha_i \Delta t}, \tag{50}$$

$$\mathbf{u}^{i+1} = \mathbf{u}^* - \alpha_i \Delta t \nabla \hat{p}, \tag{51}$$

$$p^{i+1} = p^i + \hat{p} - \frac{\alpha_i \Delta t}{2} \frac{Sc}{Pe} \nabla^2 \hat{p}. \tag{52}$$

enddo

For the case of phoretic particle, the concentration boundary condition C_I is obtained from Equation 39*a*,*b* and the velocity boundary U^b is based in Equation (8). The forcing term of concentration field for Neumann boundary condition is calculated at the two inner probes while the force for the velocity boundary condition is still added at the surface Lagrangian points. The slip velocity is calculated with the concentration at neighboring Lagrangian grids, and the procedure is detailed in Appendix.

The motion of the particles is advanced by the same method (Equation (26)) in the previous section. In this manuscript, we assume $\rho_f / \rho_p = 2$ and $I_p = \rho_p \pi L^5 / 60$. Note that due to rotation of the particle, the relative position vector of the Lagrangian point and center of the particle $\mathbf{r}_l^i = \mathbf{X}_l^i - \mathbf{x}_c^i$ is independent of time. The force and torque exerted on the particle involves two parts: the Lagrangian force on the surface of the particle and the change of momentum/angular momentum inside the particle [41].

Comparing the original and the improved method, the difference is that we calculate the force *corrections* to the forces of the last time step, in contrast to the traditional method of calculating the full forces in each time step. As mentioned before, this method is analogous to the pressure correction in fractional step methods [58] which are widely used in last three decades in comparison to the total pressure calculation from the original projection method [70]. It is important to also note that the improved method does not require any additional computational cost and it can be efficiently implemented into various direct-forcing IBM to enhance the boundary condition satisfaction.

3. Results

In this section, we present various numerical examples to showcase the enhancements brought about by the new method, highlighting its capability in simulating scenarios involving phoretic particles.

3.1. Phoretic particle

3.1.1. Particle with constant concentration at the surface

We first test the new forcing scheme by solving the three-dimensional diffusion problem from a sphere with unit diameter in a cubic box with both the original and the improved method. The simulations are performed in a cubic box of size $10 \times 10 \times 10$ with a uniform mesh of $192 \times 192 \times 192$ points. The surface of the sphere is discretized into 5120 triangular elements and the edge of the equilateral triangles is 0.7 times the Eulerian grid spacing. The sphere is located at the center of the box. The computational box and the Lagrangian meshes are shown in Fig. 3. The reference length is the diameter of the particle. The Schmidt and Péclet numbers are selected based on the case of Janus particle in 25% volume fraction H_2O_2 solution [25]. The Schmidt number is set as $Sc = 510$ and the Péclet number is set to $Pe = 8.45 \times 10^{-3}$ [25]. The time step is fixed at $\Delta t = 10^{-4}$, which is small enough to achieve time step independent results. At the side walls of the box, the concentration is set as 0 and on the surface of the sphere, concentration is prescribed as 1. The only difference between the original and improved method lies in the forcing scheme. Fig. 4 shows the concentration distribution at Lagrangian points by the two methods after convergence. It can be seen that the error of

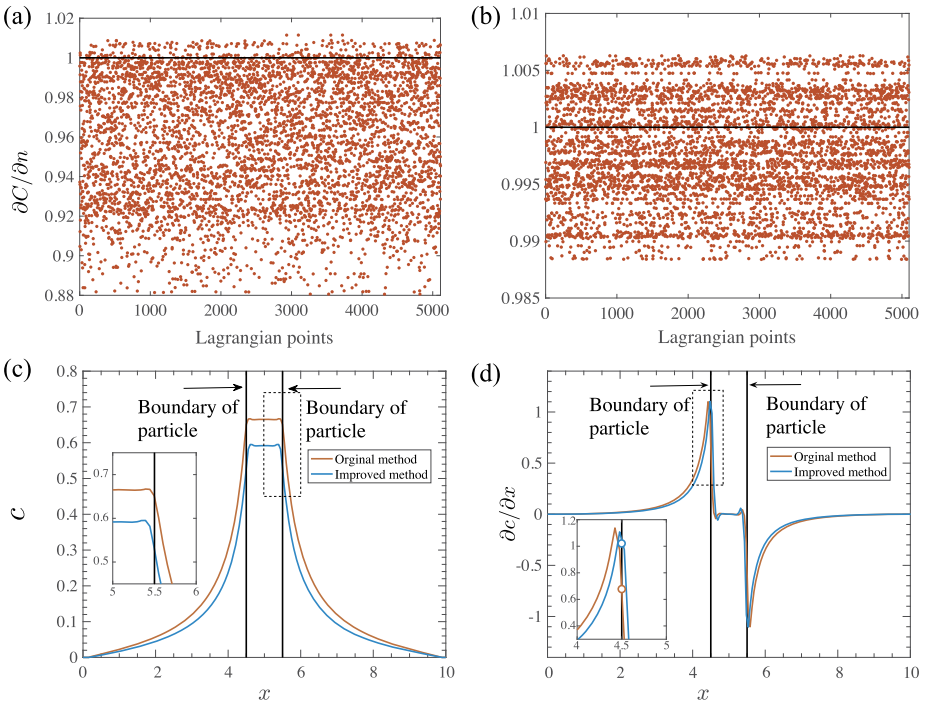

Fig. 5. (a,b) Normal concentration gradient on the surface of the isotropic phoretic particle ($\partial C/\partial n = 1$) by original method (a) and improved method (b) compared to the exact boundary condition. (c) Concentration profile along the line $y = 5, z = 5$. A zoom in at the surface is plotted in the subplot. (d) Concentration gradient component $\partial c/\partial x$ along the surface of the stationary Janus particle. A zoom in at the surface is plotted in the subplot. The parameters are $Sc = 510$ and $Pe = 8.45 \times 10^{-3}$.

the surface concentration is 2.1% for the original method while for the improved method, the error decreases to 0.4%, by applying our improvement. In the plot, we also conduct a test case employing the full explicit discretization of the diffusion term (utilizing second-order Adams-Bashforth). This test revealed even a further reduction in error; however, it was not entirely eliminated because of regularization of interpolation and spreading still cause error.

3.1.2. Fully covered catalytic particle

Here we test the two-inner-probe method for Neumann boundary condition. We solve the three-dimensional convection-diffusion problem from a phoretic sphere (with slip velocity due to diffusiophoresis) in a cubic box with both the original and the improved method. The concentration gradient at the surface is set as 1 due to the chemical reaction. All the other parameters are the same as that in the section 3.1.1.

In Fig. 5, we present a comparative analysis of results obtained using both the original and enhanced methodologies. In the case of the original method, it was observed that the gradient error was approximately 12% (as depicted in Fig. 5(a)). However, when employing the improved method, a significant enhancement was observed, reducing the error in the concentration gradient at the surface to just 1.1% (illustrated in Fig. 5(b)). This discrepancy arises from the treatment of concentration gradient continuity across the surface. To illustrate, Fig. 5(c) displays the concentration profile along the line defined by $y = 5$ and $z = 5$. In the zoomed-in subplot, we can observe that the original method only maintains concentration gradient continuity in the outward direction, whereas the improved method ensures gradient continuity in both directions, achieved through the implementation of the two-inner probe method. The difference in continuity has a notable impact on the calculation of the concentration gradient within the code. As evidenced in Fig. 5(d), the concentration gradient along the line $y = 5, z = 5$ for the original method hovers around 0.67, while the improved method closely approximates the intended unit concentration gradient. These findings affirm that the adoption of the two-inner probe method enhances surface gradient precision by establishing concentration gradient continuity in both directions near the surface.

3.1.3. Janus particle

To demonstrate that our approach also works for Neumann boundary condition, we further test the three-dimensional diffusion problem from a spherical Janus particle. For this case, Golestanian et al. [6] have derived a theoretical formulation for the concentration distribution and the theoretical velocity [6]. The theoretical dimensionless terminal velocity of a Janus particle is:

$$V_{theory} = \frac{M\alpha}{4DV_0} = 0.25, \tag{53}$$

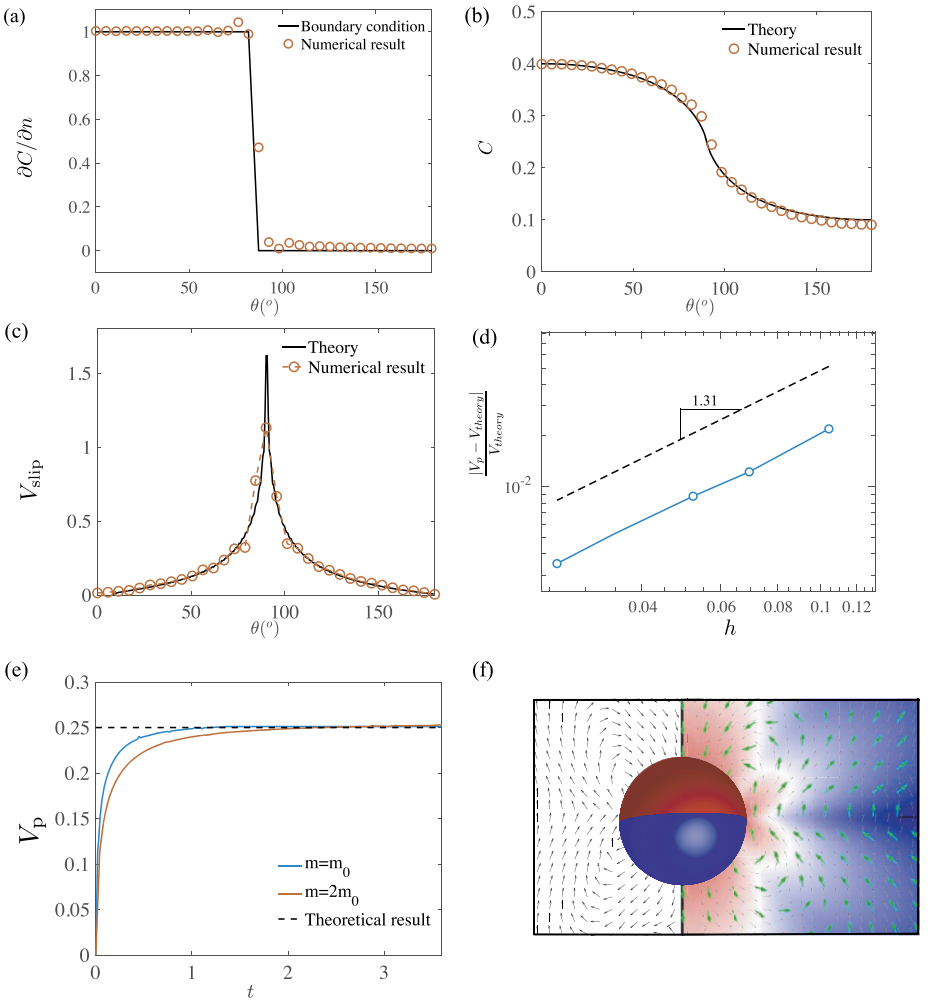

Fig. 6. Simulation result for the case of moving Janus particle. The parameters are $Sc = 510$ and $Pe = 8.45 \times 10^{-3}$. (a) Normal concentration gradient on the surface of the self-propelled Janus particle as compared to the boundary condition. (b) Concentration distribution along the surface of the self-propelled Janus particle. (c) Slip velocity distribution along the surface of the self-propelled Janus particle. The solid lines in (a-c) represents the theoretical results [6]. (d) Error of terminal velocity as a function of grid resolution h. (e) Time evolution for the velocity of the self-propelled Janus particle. (f) Streamlines from the present result as compared to that from [71]. The streamline on the left is our present results and the one on the right is from [71].

where $V_0 = \frac{M\alpha}{D}$ is the characteristic velocity.

Here we show that our numerical results agree very well with the theoretical result under the same conditions, see Fig. 6(a) for the satisfaction of the Neumann boundary condition, Fig. 6(b) for the concentration average C in azimuthal direction, and Fig. 6(c) for the comparison on the slip velocity along the surface between the numerical simulation and the theory. It is seen that our current approach can indeed make the concentration gradient smooth enough along the boundary. The terminal velocity also converge to the theoretical velocity V_{theory}. We plot the error $\frac{V_p - V_{theory}}{V_{theory}}$ as function of grid size h in Fig. 6(d). The order of grid convergence is around 1.31. Furthermore, we perform a mass independent test in Fig. 6 (e) to show that the terminal velocity is the same for different masses, which agrees with the theoretical result. Last but not least, in Fig. 6 (f) we compare the velocity vectors obtained from our simulation with the one from [71] which adopted a cylindrical coordinate and it can be seen that good agreement can be found between the two studies.

3.2. Three-dimensional flow past a fixed sphere

In order to show that the proposed method performs equally well also with standard canonical benchmarks, we present here the well studied case of the flow past a sphere with no-slip boundary conditions. The computations are performed in the domain of $L_x \times L_y \times L_z = 10 \times 10 \times 38$, where l_z is the streamwise length. A uniform inflow comes from z direction and out-flow boundary condition is applied at outlet. The sphere of unit diameter is located at $(5, 5, 3)$. A mesh of uniform size 0.015 is generated in the vicinity the sphere $(1.5 \times 1.5 \times 1.5)$. The total grid resolution is $359 \times 359 \times 431$. The control parameter of the system is the Reynolds

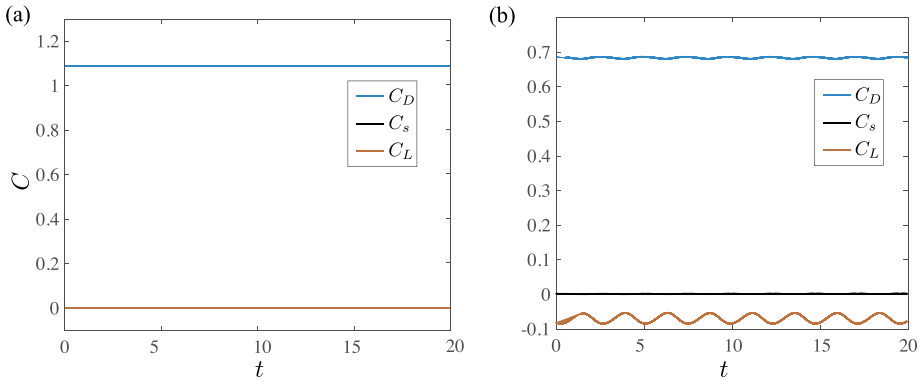

Fig. 7. Time history of the side force C_s, drag C_D and lift C_L coefficients for flow over sphere at (a) Re = 100 and (b) Re = 300.

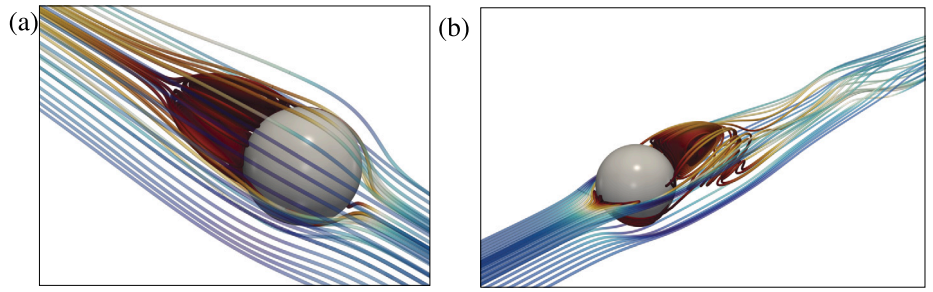

Fig. 8. (a,b) Instantaneous three dimensional streamlines for flow over a sphere at (a) $Re = 100$ and (b) $Re = 300$. Colors denote the vorticity at the coordinates.

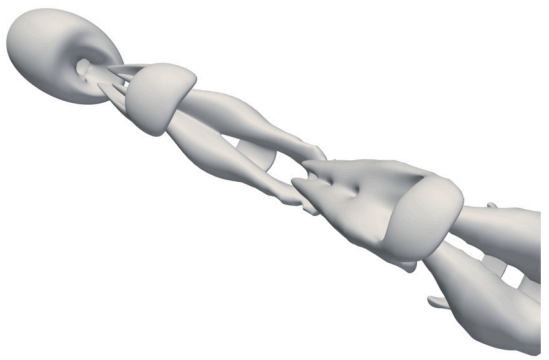

Fig. 9. Instantaneous vortical structure of flow past a sphere at $Re = 300$.

number $Re = UL/\nu$, where U is the inflow velocity and L is the sphere diameter. Here we consider two Reynolds numbers, $Re = 100$ and 300, the domain size is the same for the two Reynolds number.

The side force, drag and lift coefficients are defined as

$$C_s = \frac{F_s}{1/2\rho U^2 L}, \quad C_D = \frac{F_D}{1/2\rho U^2 L}, \quad C_L = \frac{F_l}{1/2\rho U^2 L}, \tag{54a,b,c}$$

where F_s, F_D and F_l are the time-averaged side, drag and lift forces. After the system reaches a statistical steady state, the side force, drag and lift coefficients are shown in Fig. 7. The comparisons of the present simulations with those from the literature are shown in Table 1. For both $Re = 100$ and $Re = 300$ cases, our results are in excellent agreement with those from the literature.

At $Re = 100$, the flow is axis-symmetric and steady. A stable separation bubble is generated, while at $Re = 300$, the flow is unsteady with vortex shedding; see Fig. 8 (a, b) for the instantaneous streamlines. Furthermore, we plot the streamlines at the $y - z$ plane of $x = 5$ for both cases $Re = 100$ and $Re = 300$ in Fig. 10. We further show a visualization of the vortical structures for the case $Re = 300$ in Fig. 9, with vortex identification method of [77]. It can be seen that the vortical structure is nearly the same as that in [63,72]. Table 2 shows good agreement between the current results and previous literature for separation angle θ length l and vortex position measured by a and b.

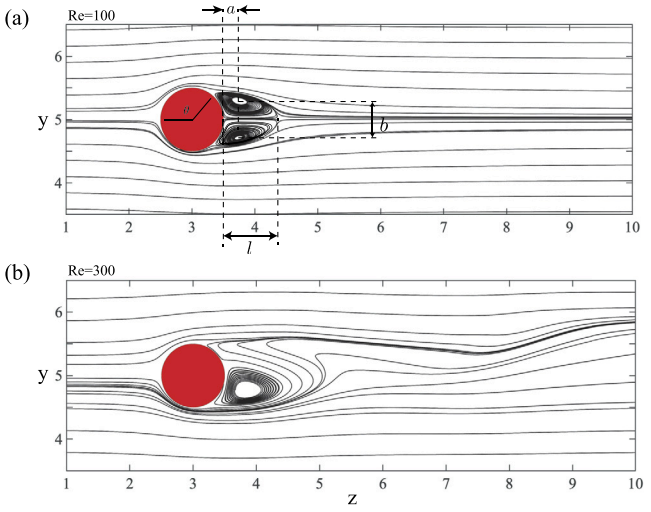

Fig. 10. (a,b) Instantaneous streamlines on the y-z middle plane for flow over a sphere at (a) $Re = 100$ and (b) $Re = 300$.

Table 1
Drag and lift coefficient for flow past sphere at $Re = 100$ and 300.

$Re = 100$	C_D	$Re = 300$	C_D	C_L
Fornberg (1988) [72]	1.085	Ploumhans et al. (2002) [73]	0.683	−0.061
Fadlun et al. (2000) [57]	1.079	Johnson and Patel (1999) [74]	0.656	−0.069
Kim et al (2001) [49]	1.087			
Present result	1.086	Present result	0.684	−0.0695

Table 2
The separation length l and vortex position measured by a and b and separation angle θ for flow past sphere at $Re = 100$. The definitions of the parameters can be found in Fig. 10.

$Re = 100$	l	a	b	θ
Magnaudet et al.(1995) [75]	0.847	-	-	-
Taneda (1956, experiment) [76]	0.899	-	-	127.5
Johnson and Patel (1999) [74]	0.84	0.258	0.58	125.5
present result	0.843	0.248	0.58	126.4

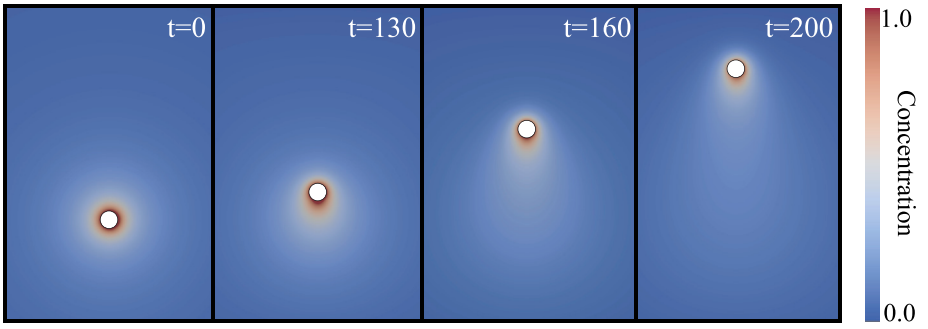

Fig. 11. From left to right: The time series of an isotropic phoretic particle with $Sc = 1$, $Pe = 10$. It can be seen that a spontaneously symmetry breaking happens and drives the motion of the particle. The color bar denotes the value of the concentration.

3.3. Spontaneously symmetry breaking of an isotropic phoretic particle

Michelin et al. [24] proposed that even for an isotropic phoretic particle, the system can break the symmetry and a spontaneous self-propelled motion can be induced when $Pe > 4$. Here we perform several simulations with different Pe and fixed $Sc = 1$. The computational settings are the same as those for the Janus particle simulations except the particle is fully covered by the catalyst with the same boundary condition $\partial C/\partial n = 1$. The radius of the particle is set as characteristic length in this section to keep the Pe

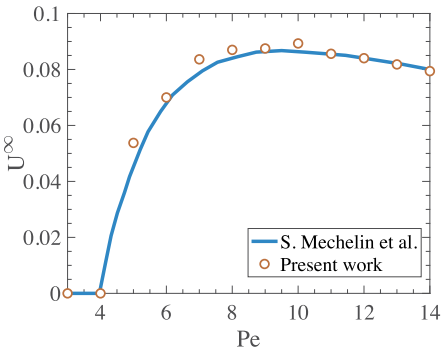

Fig. 12. Variations of terminal velocity with Pe for an isotropic phoretic particle at $Sc = 1$.

definition the same as that in [24]. Note that in [24], body fitted meshes are used and the equations are solved in a comoving frame of reference. Fig. 11 shows the time series of concentration field for isotropic particle with $Sc = 1, Pe = 10$. It can be seen that the a spontaneous movement of particle is generated. We further show in Fig. 12 the comparison of the terminal velocity at different Pe between our results and those from [24]: The terminal velocity agrees very well between the two studies.

4. Conclusions

In this paper, an improved direct-forcing immersed boundary method is developed for Dirichlet and Neumann boundary conditions for the applications to phoretic particles in fluids. The forcing method and the Neumann boundary condition implementation is simple and straightforward, thus it can be implemented into many variations of the direct forcing methods. The immersed boundary method is combined with a powerful open-source code AFiD, which can be potentially applied to a wide range of flows. The method has been validated by several problems with different complexity, including the pure diffusion equation, self-propelled Janus particle, flow past a sphere and spontaneously symmetry breaking of an isotropic phoretic particle. Excellent agreements are found between the results from our simulations and those from the literature.

CRediT authorship contribution statement

Xiaojue Zhu: Conceptualization, Formal analysis, Methodology, Validation, Visualization, Writing – original draft, Writing – review & editing. **Yibo Chen:** Data curation, Formal analysis, Investigation, Methodology, Validation, Visualization, Writing – original draft, Writing – review & editing. **Kai Leong Chong:** Methodology, Validation, Writing – original draft, Writing – review & editing. **Detlef Lohse:** Conceptualization, Funding acquisition, Project administration, Supervision, Writing – original draft, Writing – review & editing. **Roberto Verzicco:** Conceptualization, Project administration, Supervision, Writing – original draft, Writing – review & editing.

Declaration of competing interest

The authors declare that they have no known competing financial interests or personal relationships that could have appeared to influence the work reported in this paper.

Data availability

Data will be made available on request.

Acknowledgements

We acknowledge the support from the Netherlands Center for Multiscale Catalytic Energy Conversion (MCEC), an NWO Gravitation program funded by the Ministry of Education and support from the ERC-Advanced Grant “DDD” under the project number 740479. The simulations in this work were carried out on the national e-infrastructure of SURFsara, a subsidiary of SURF cooperation, the collaborative ICT organization for Dutch education and research, MareNostrum 4 which is based in Spain at the Barcelona Computing Center (BSC) under PRACE projects 2018194742, 2020225335 and 2020235589, on Irene at Trés Grand Centre de calcul

du CEA (TGCC) under PRACE project 2019215098 and on Marconi successor at CINECA, Italy under PRACE project 2019204979. X. Z. acknowledges the support from the Max Planck Society, DFG grants 521319293 and 540422505, and the Alexander von Humboldt-Stiftung.

Appendix A. Numerical calculation of slip velocity

The slip velocity of the phoretic particle is driven by the concentration gradient (Equation (7)). Fig. A.13 shows triangular Lagrangian elements. For the concentration gradient ∇C, i.e. $\partial C/\partial x, \partial C/\partial y, \partial C/\partial z$ at the centroid of triangle 0, we have to use the surrounding three triangles $1, 2, 3$, with the following equations:

$$\nabla C \cdot \hat{i}_{01} = \nabla C_{01} = \frac{C_1 - C_0}{d_{01}}, \tag{A.1}$$

$$\nabla C \cdot \hat{i}_{02} = \nabla C_{02} = \frac{C_2 - C_0}{d_{02}}, \tag{A.2}$$

$$\nabla C \cdot \hat{i}_{03} = \nabla C_{03} = \frac{C_3 - C_0}{d_{03}}, \tag{A.3}$$

where $\hat{i}_{ij}$ and d_{ij} are the unit vector in the direction from center of triangle i to the center of triangle j and distance between the two points, respectively. C_i the concentration at the center of triangle i. Using Equation (7) we can then obtain the slip velocity. Fig. 6(c) shows the good agreement on the slip velocity between the numerical results and the theoretic prediction. Note that in this manuscript we only deal with non-deformable spheres. For deformable spheres, surface triangulations are not always as smooth as in Fig. A.13 and more tests are needed for the calculations of surface gradients.

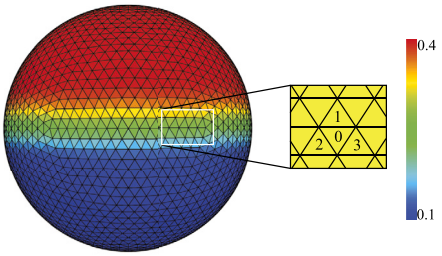

Fig. A.13. Sketch of the four neighboring triangles that are used to calculate the three components for the concentration gradient at point 0 of a Janus particle. The colormap is based on the local concentration.

References

[1] S. Ramaswamy, The mechanics and statistics of active matter, Annu. Rev. Condens. Matter Phys. 1 (2010) 323–345.
[2] M.C. Marchetti, J.F. Joanny, S. Ramaswamy, T.B. Liverpool, J. Prost, M. Rao, R.A. Simha, Hydrodynamics of soft active matter, Rev. Mod. Phys. 85 (2013) 1143.
[3] E. Lauga, Bacterial hydrodynamics, Annu. Rev. Fluid Mech. 48 (2016) 105–130.
[4] D. Needleman, Z. Dogic, Active matter at the interface between materials science and cell biology, Nat. Rev. Mater. 2 (9) (2017) 17048.
[5] A. Doostmohammadi, J. Ignés-Mullol, J.M. Yeomans, F. Sagués, Active nematics, Nat. Commun. 9 (2018) 1–13.
[6] R. Golestanian, T. Liverpool, A. Ajdari, Designing phoretic micro- and nano-swimmers, New J. Phys. 9 (5) (2007) 126.
[7] J.L. Moran, J.D. Posner, Phoretic self-propulsion, Annu. Rev. Fluid Mech. 49 (2017) 511–540.
[8] P. Illien, R. Golestanian, A. Sen, 'Fuelled' motion: phoretic motility and collective behaviour of active colloids, Chem. Soc. Rev. 46 (2017) 5508–5518.
[9] S. Michelin, Self-propulsion of chemically active droplets, Annu. Rev. Fluid Mech. 55 (2023) 77–101.
[10] A. Walther, A.H.E. Muller, Janus particles: synthesis, self-assembly, physical properties, and applications, Chem. Rev. 113 (2013) 5194–5261.
[11] C.C. Maass, C. Krüger, S. Herminghaus, C. Bahr, Swimming droplets, Annu. Rev. Condens. Matter Phys. 7 (2016) 171–193.
[12] B. ten Hagen, S. van Teeffelen, H. Löwen, Brownian motion of a self-propelled particle, J. Phys. Condens. Matter 23 (2011) 194119.
[13] I. Buttinoni, G. Volpe, F. Kümmel, G. Volpe, C. Bechinger, Active Brownian motion tunable by light, J. Phys. Condens. Matter 24 (2012) 284129.
[14] P.K. Ghosh, V.R. Misko, F. Marchesoni, F. Nori, Self-propelled Janus particles in a ratchet: numerical simulations, Phys. Rev. Lett. 110 (2013) 268301.
[15] X. Zheng, B. ten Hagen, A. Kaiser, M. Wu, H. Cui, Z. Silber-Li, H. Löwen, Non-Gaussian statistics for the motion of self-propelled Janus particles: experiment versus theory, Phys. Rev. E 88 (2013) 032304.
[16] A. Rashidi, S. Razavi, C.L. Wirth, Influence of cap weight on the motion of a janus particle very near a wall, Phys. Rev. E 101 (4) (2020) 042606.
[17] J.F. Brady, Particle motion driven by solute gradients with application to autonomous motion: continuum and colloidal perspectives, J. Fluid Mech. 667 (2011) 216–259.
[18] H. Rezvantalab, S. Shojaei-Zadeh, Tilting and tumbling of Janus nanoparticles at sheared interfaces, ACS Nano 10 (2016) 5354–5361.
[19] J. Koplik, C. Maldarelli, Molecular dynamics study of the translation and rotation of amphiphilic Janus nanoparticles at a vapor-liquid surface, Phys. Rev. Fluids 4 (2019) 044201.
[20] M.Á.G. Maestre, R. Fantoni, A. Giacometti, A. Santos, Janus fluid with fixed patch orientations: theory and simulations, J. Chem. Phys. 138 (2013) 094904.
[21] T. Baier, S. Tiwari, S. Shrestha, A. Klar, S. Hardt, Thermophoresis of Janus particles at large Knudsen numbers, Phys. Rev. Fluids 3 (2018) 094202.
[22] J.T. Padding, A.A. Louis, Hydrodynamic interactions and Brownian forces in colloidal suspensions: coarse-graining over time and length scales, Phys. Rev. E 74 (2006) 031402.
[23] M. Yang, A. Wysocki, M. Ripoll, Hydrodynamic simulations of self-phoretic microswimmers, Soft Matter 10 (2014) 6208–6218.
[24] S. Michelin, E. Lauga, D. Bartolo, Spontaneous autophoretic motion of isotropic particles, Phys. Fluids 25 (2013) 061701.

[25] F. Yang, S. Qian, Y. Zhao, R. Qiao, Self-diffusiophoresis of Janus catalytic micromotors in confined geometries, Langmuir 32 (2016) 5580–5592.
[26] W. Hu, T. Lin, S. Rafai, C. Misbah, Chaotic swimming of phoretic particles, Phys. Rev. Lett. 123 (2019) 238004.
[27] T.-S. Lin, W.-F. Hu, C. Misbah, A direct Poisson solver in spherical geometry with an application to diffusiophoretic problems, J. Comput. Phys. 409 (2020) 109362.
[28] R. Kohl, E. Corona, V. Cheruvu, S. Veerapaneni, Fast and accurate solvers for simulating janus particle suspensions in Stokes flow, Adv. Comput. Math. 49 (4) (2023) 45.
[29] Y. Chen, K.L. Chong, L. Liu, R. Verzicco, D. Lohse, Instabilities driven by diffusiophoretic flow on catalytic surfaces, J. Fluid Mech. 919 (2021) A10.
[30] Y. Chen, K.L. Chong, H. Liu, R. Verzicco, D. Lohse, Buoyancy-driven attraction of active droplets, arXiv preprint, arXiv:2302.14008, 2023.
[31] C.S. Peskin, Flow patterns around heart valves: a numerical method, J. Comput. Phys. 10 (1972) 252–271.
[32] G. Iaccarino, R. Verzicco, Immersed boundary technique for turbulent flow simulations, Appl. Mech. Rev. 56 (2003) 331–347.
[33] R. Mittal, G. Iaccarino, Immersed boundary methods, Annu. Rev. Fluid Mech. 37 (2005) 239–261.
[34] F. Sotiropoulos, X. Yang, Immersed boundary methods for simulating fluid–structure interaction, Prog. Aerosp. Sci. 65 (2014) 1–21.
[35] R. Verzicco, Immersed boundary methods: historical perspective and future outlook, Annu. Rev. Fluid Mech. 55 (2023) 129–155.
[36] X. Zhu, G. He, X. Zhang, Numerical study on hydrodynamic effect of flexibility in a self-propelled plunging foil, Comput. Fluids 97 (2014) 1–20.
[37] X. Zhu, G. He, X. Zhang, Flow-mediated interactions between two self-propelled flapping filaments in tandem configuration, Phys. Rev. Lett. 113 (2014) 238105.
[38] F.-B. Tian, H. Dai, H. Luo, J.F. Doyle, B. Rousseau, Fluid–structure interaction involving large deformations: 3D simulations and applications to biological systems, J. Comput. Phys. 258 (2014) 451–469.
[39] M.D. de Tullio, G. Pascazio, A moving-least-squares immersed boundary method for simulating the fluid–structure interaction of elastic bodies with arbitrary thickness, J. Comput. Phys. 325 (2016) 201–225.
[40] M. Uhlmann, An immersed boundary method with direct forcing for the simulation of particulate flows, J. Comput. Phys. 209 (2005) 448–476.
[41] W.P. Breugem, A second-order accurate immersed boundary method for fully resolved simulations of particle-laden flows, J. Comput. Phys. 231 (2012) 4469–4498.
[42] T. Kempe, J. Fröhlich, An improved immersed boundary method with direct forcing for the simulation of particle laden flows, J. Comput. Phys. 231 (2012) 3663–3684.
[43] V. Spandan, V. Meschini, R. Ostilla-Mónico, D. Lohse, G. Querzoli, M.D. de Tullio, R. Verzicco, A parallel interaction potential approach coupled with the immersed boundary method for fully resolved simulations of deformable interfaces and membranes, J. Comput. Phys. 348 (2017) 567–590.
[44] V. Mathai, X. Zhu, C. Sun, D. Lohse, Mass and moment of inertia govern the transition in the dynamics and wakes of freely rising and falling cylinders, Phys. Rev. Lett. 119 (2017) 054501.
[45] J. Yuan, U. Piomelli, Estimation and prediction of the roughness function on realistic surfaces, J. Turbul. 15 (2014) 350–365.
[46] X. Zhu, R. Ostilla-Mónico, R. Verzicco, D. Lohse, Direct numerical simulation of Taylor–Couette flow with grooved walls: torque scaling and flow structure, J. Fluid Mech. 794 (2016) 746–774.
[47] X. Zhu, R. Verzicco, D. Lohse, Disentangling the origins of torque enhancement through wall roughness in Taylor–Couette turbulence, J. Fluid Mech. 812 (2017) 279–293.
[48] X. Zhu, R.A. Verschoof, D. Bakhuis, S.G. Huisman, R. Verzicco, C. Sun, D. Lohse, Wall roughness induces asymptotic ultimate turbulence, Nat. Phys. 14 (2018) 417.
[49] J. Kim, H. Choi, An immersed-boundary finite-volume method for simulation of heat transfer in complex geometries, KSME Int. J. 18 (2004) 1026–1035.
[50] N. Zhang, Z.C. Zheng, S. Eckels, Study of heat-transfer on the surface of a circular cylinder in flow using an immersed-boundary method, Int. J. Heat Fluid Flow 29 (2008) 1558–1566.
[51] W. Ren, C. Shu, W. Yang, An efficient immersed boundary method for thermal flow problems with heat flux boundary conditions, Int. J. Heat Mass Transf. 64 (2013) 694–705.
[52] K. Luo, Z. Zhuang, J. Fan, N.E.L. Haugen, A ghost-cell immersed boundary method for simulations of heat transfer in compressible flows under different boundary conditions, Int. J. Heat Mass Transf. 92 (2016) 708–717.
[53] Y. Wang, C. Shu, L. Yang, Boundary condition-enforced immersed boundary-lattice Boltzmann flux solver for thermal flows with Neumann boundary conditions, J. Comput. Phys. 306 (2016) 237–252.
[54] X. Zhu, R.J.A.M. Stevens, R. Verzicco, D. Lohse, Roughness-facilitated local 1/2 scaling does not imply the onset of the ultimate regime of thermal convection, Phys. Rev. Lett. 119 (2017) 154501.
[55] F. Toja-Silva, J. Favier, A. Pinelli, Radial basis function (rbf)-based interpolation and spreading for the immersed boundary method, Comput. Fluids 105 (2014) 66–75.
[56] B. Wu, J. Lu, H. Lee, C. Shu, M. Wan, An explicit boundary condition-enforced immersed boundary-reconstructed thermal lattice Boltzmann flux solver for thermal–fluid–structure interaction problems with heat flux boundary conditions, J. Comput. Phys. 485 (2023) 112106.
[57] E.A. Fadlun, R. Verzicco, P. Orlandi, J. Mohd-Yusof, Combined immersed-boundary finite-difference methods for three-dimensional complex flow simulations, J. Comput. Phys. 161 (2000) 35–60.
[58] J. Kim, P. Moin, Application of a fractional-step method to incompressible Navier-Stokes equations, J. Comput. Phys. 59 (1985) 308–323.
[59] S. Gsell, U. d'Ortona, J. Favier, Explicit and viscosity-independent immersed-boundary scheme for the lattice Boltzmann method, Phys. Rev. E 100 (3) (2019) 033306.
[60] S. Gsell, J. Favier, Direct-forcing immersed-boundary method: a simple correction preventing boundary slip error, J. Comput. Phys. 435 (2021) 110265.
[61] V. Spandan, D. Lohse, M.D. de Tullio, R. Verzicco, A fast moving least squares approximation with adaptive Lagrangian mesh refinement for large scale immersed boundary simulations, J. Comput. Phys. 375 (2018) 228–239.
[62] M.M. Rai, P. Moin, Direct simulations of turbulent flow using finite-difference schemes, J. Comput. Phys. 96 (1991) 15–53.
[63] S. Wang, X. Zhang, An immersed boundary method based on discrete stream function formulation for two- and three-dimensional incompressible flows, J. Comput. Phys. 230 (2011) 3479–3499.
[64] R. Verzicco, P. Orlandi, A finite-difference scheme for three-dimensional incompressible flows in cylindrical coordinates, J. Comput. Phys. 123 (1996) 402–414.
[65] E.P. van der Poel, R. Ostilla-Mónico, J. Donners, R. Verzicco, A pencil distributed finite difference code for strongly turbulent wall-bounded flows, Comput. Fluids 116 (2015) 10–16.
[66] X. Zhu, E. Phillips, V. Spandan, J. Donners, G. Ruetsch, J. Romero, R. Ostilla-Mónico, Y. Yang, D. Lohse, R. Verzicco, M. Fatica, R.J.A.M. Stevens, AFiD-GPU: a versatile Navier–Stokes solver for wall-bounded turbulent flows on GPU clusters, Comput. Phys. Commun. 229 (2018) 199–210.
[67] X. Zhu, R.J.A.M. Stevens, O. Shishkina, R. Verzicco, D. Lohse, $Nu \sim Ra^{1/2}$ Scaling enabled by multiscale wall roughness in Rayleigh–Bénard turbulence, J. Fluid Mech. 869 (2019) R4.
[68] S.H. Bader, X. Zhu, Scaling relations in quasi-static magnetoconvection with a strong vertical magnetic field, J. Fluid Mech. 976 (2023) A4.
[69] J. Song, O. Shishkina, X. Zhu, Scaling regimes in rapidly rotating thermal convection at extreme Rayleigh numbers, J. Fluid Mech. 984 (2024) A45.
[70] A.J. Chorin, Numerical solution of the Navier-Stokes equations, Math. Comput. 22 (1968) 745–762.
[71] J. de Graaf, G. Rempfer, C. Holm, Diffusiophoretic self-propulsion for partially catalytic spherical colloids, IEEE Trans. Nanobiosci. 14 (2015) 272–288.
[72] B. Fornberg, Steady viscous flow past a sphere at high Reynolds numbers, J. Fluid Mech. 190 (1988) 471–489.
[73] P. Ploumhans, G.S. Winckelmans, J.K. Salmon, A. Leonard, M.S. Warren, Vortex methods for direct numerical simulation of three-dimensional bluff body flows: application to the sphere at Re = 300, 500, and 1000, J. Comput. Phys. 178 (2002) 427–463.

[74] T.A. Johnson, V.C. Patel, Flow past a sphere up to a Reynolds number of 300, J. Fluid Mech. 378 (1999) 19–70.
[75] J. Magnaudet, M. Rivero, J. Fabre, Accelerated flows past a rigid sphere or a spherical bubble. Part 1. Steady straining flow, J. Fluid Mech. 284 (1995) 97–135.
[76] S. Taneda, Experimental investigation of the wake behind a sphere at low Reynolds numbers, J. Phys. Soc. Jpn. 11 (10) (1956) 1104–1108.
[77] J. Jeong, F. Hussain, On the identification of a vortex, J. Fluid Mech. 285 (1995) 69–94.